Environmental Pollution 280 (2021) 116974

Contents lists available at ScienceDirect

Environmental Pollution

journal homepage: www.elsevier.com/locate/envpol

# Tissue distribution of polystyrene nanoplastics in mice and their entry, transport, and cytotoxicity to GES-1 cells☆

Yunfei Ding [1], Ruiqing Zhang [1], Boqing Li, Yunqiu Du, Jing Li, Xiaohan Tong, Yulong Wu, Xiaofei Ji, Ying Zhang*

*School of Basic Medical Sciences, Binzhou Medical University, Yantai, 264003, China*

ARTICLE INFO

*Article history:*
Received 16 November 2020
Received in revised form
12 February 2021
Accepted 16 March 2021
Available online 19 March 2021

*Keywords:*
Nanoplastics
Endocytosis
Proliferation
Apoptosis
Autophagy

ABSTRACT

With the widespread use of plastics and nanotechnology products, nanoplastics (NPs) have become a potential threat to human health. It is of great practical significance to study and evaluate the distribution of NPs in mice as mammal models and their entry, transport, and cytotoxicity in human cell lines. In this study, we detected the tissue distribution of fluorescent polystyrene nanoplastics (PS-NPs) in mice and assessed their endocytosis, transport pathways, and cytotoxic effects in GES-1 cells. We found that PS-NPs were clearly visible in gastric, intestine, and liver tissues of mice and in GES-1 cells treated with PS-NPs. Entry of PS-NPs into GES-1 cells decreased with the inhibition of caveolae-mediated endocytosis (nystatin), clathrin-mediated endocytosis (chlorpromazine HCl), micropinocytosis (ethyl-isopropyl amiloride), RhoA (CCG-1423), and F-actin polymerization (lantrunculin A). Rac1 inhibitors (NSC 23766) had no significant effect on PS-NPs entering GES-1 cells. F-actin levels significantly decreased in CCG-1423-pretreated GES-1 cells exposed to PS-NPs. GES-1 cell ultrastructural features indicated that internalized PS-NPs can be encapsulated in vesicles, autophagosomes, lysosomes, and lysosomal residues. RhoA, F-actin, RAB7, and LAMP1 levels in PS-NPs-treated GES-1 cells were remarkably up-regulated and the Rab5 level was significantly down-regulated compared to levels in untreated cells. PS-NPs treatment decreased cell proliferation rates and increased cell apoptosis. The formation of autophagosomes and autolysosomes and levels of LC3II increased with the length of PS-NPs treatment. The results indicated that cells regulated endocytosis in response to PS-NPs through the RhoA/F-actin signaling pathway and internalized PS-NPs in the cytoplasm, autophagosomes, or lysosomes produced cytotoxicity. These results illustrate the potential threat of NPs pollution to human health.

## 1. Introduction

Nanoplastics (NPs), which are defined as plastic debris with a diameter of <100 nm (Gewert et al., 2015; Gigault et al., 2018), accumulate in the environment due to the degradation of plastics by ultraviolet rays and microorganisms (Song et al., 2017; Yousif and Haddad, 2013; Wilkinson et al., 2017), and direct release from electronic products, food packages (Eleftheriadou et al., 2017), personal care products, and textiles (Contado, 2015). The human body is exposed to NPs mainly through ingestion of food and water, inhalation of air, and direct skin contact with NPs, but ingestion is considered to be the main path of exposure (Domenech et al., 2020; Prata, 2018). Although not visible to the human eye, NPs are everywhere and pose a potential threat to human health.

Previous studies have shown that smaller sized NPs can be absorbed more easily, and they tend to be more toxic to organisms (Lu et al., 2016). Kashiwada (2006) reported that polystyrene NPs (PS-NPs) (39.4 nm, 10 mg/L) can be ingested by the Japanese rice fish (*Oryzias latipes*) and distributed in their gills, viscera, and blood. Similarly, Lu et al. (2016) documented the intake and accumulation of PS-NPs (70 nm) in the liver of zebrafish (*Danio rerio*) treated with 20 μg/L ($1.1 \times 10^8$ particles/mL) of PS-NPs. In mammals, PS-NPs were ingested and found in the intestinal epithelium of female rats 5 d after gavage with 60 nm PS-NPs, and absorption rates up to 10% were reported (Hillery et al., 1994). Therefore, understanding the uptake of NPs in the gastric and intestine tissue of mice and how they migrate across the gastrointestinal (GI) barrier to other

---

☆ This paper has been recommended for acceptance by Maria Cristina Fossi.

* Corresponding author. 19# Jianan Road, Yantai, 264003, China.
*E-mail address:* zhangying@bzmu.edu.cn (Y. Zhang).

[1] These authors contributed equally to the paper.

https://doi.org/10.1016/j.envpol.2021.116974

tissues will help us understand the potential hazard of NPs in humans.

In vitro studies of NPs have focused on macrophages (Kuhn et al., 2014) and other epithelial cells (liver, lung, and intestine) (Busch et al., 2021; He et al., 2020; Xu et al., 2019). He et al. (2020) found that 50 nm PS-NPs internalized and accumulated in HepG2 cells, induced oxidative stress, reduced antioxidant capacity, and resulted in 25–48% cell death. A549 cells treated with PS-NPs (25 nm and 70 nm) exhibited apoptosis and inflammation, disrupted membrane integrity, and cell necrosis (Xu et al., 2019). Busch et al. (2021) reported that PS-NPs (50 nm) induced membrane disruption, lysed lysosomes, and greatly reduced cell metabolic viability in Caco-2 cells. With a surface area of about 200 $m^2$, the GI tract is the primary point of contact for ingestion of NPs, and it is responsible for nutrient transport and absorption (Lehner et al., 2019). However, microbial flora in the intestine can degrade NPs into multiple sizes and structures, and might influence the ways in which NPs enter small intestine tissues (Walczak et al., 2015). It also is particularly important to study the entry, transport, and cytotoxicity of NPs to gastric epithelial (GES-1) cells.

The goals of this study were to (1) detect the tissue distribution of PS-NPs in mice, (2) elucidate the entry and transport mechanisms of PS-NPs in GES-1 cells, and (3) assess the effect of PS-NPs on cell proliferation, apoptosis, and autophagy. The results of this study will provide theoretical support for evaluating the impact of NPs pollution on human health.

## 2. Materials and methods

### 2.1. Animal care and experimental scheme

Five-week-old SPF grade C57BL/6 male mice were obtained from the Jinan Pengyue Laboratory Animal Breeding Company (Jinan, China; license key: SCXK (Lu) 20140007). Fluorescent PS-NPs ($d = 60$ nm) with an excitation wavelength of 488 nm and an emission wavelength of 520 nm were purchased from the Bangs Laboratories (Fishers, IN, USA). Before the experiments began, the mice were housed at $25 \pm 4$ °C for 1 week.

Mice were assigned to two groups ($n = 6$ for each group) named PS and Blank. In the PS group, all mice were intragastrically inoculated with 50 μg/mL PS-NPs (500 μL), which were dissolved in $ddH_2O$ (Deng et al., 2017). In the Blank group, the mice were inoculated with $ddH_2O$ without PS-NPs. Three days later, gastric, intestine, liver, cardiac, spleen, and lung tissues were rapidly harvested. All studies involving mice were licensed by the Animal Care and Use Committee of the Binzhou Medical University (Yantai, China).

### 2.2. Immunofluorescence staining of cryo-sections

One part of the gastric, intestine, liver, cardiac, spleen, and lung tissues was placed in 4% paraformaldehyde, dehydrated with 30% sucrose solution, and embedded into optimal cutting temperature compound. Sections of 10 μm thickness were prepared and sliced using an HM525 NX Cryostat (Thermo Fisher Scientific, Waltham, MA, USA) (Son et al., 2013).

The slices were dried at room temperature and stained with 4′,6′-diamidino-2-phenylindole (DAPI) for 20 min, then mounted using an anti-fluorescent quench sealant. Images were obtained with a confocal laser scanning microscope (Leica TCS SPE, Wetzlar, Germany) (350 nm for DAPI; 488 nm for the green PS-NPs).

### 2.3. Transmission electron microscopy

The other part of the gastric, intestine, liver, cardiac, spleen, and lung tissues and GES-1 cells treated with PS-NPs for 3 h were all fixed with 2.5% glutaraldehyde and postfixed with 1% osmium. The samples were dehydrated by ethanol, rinsed in acetone, and then embedded in epoxy resin (Tizro et al., 2019). The embedded samples were sliced to 50–60 nm thickness using an Leica UC7 ultramicrotome (Leica, Wetzlar, Germany). Ultra-thin slices were stained with 2% lead citrate and uranyl acetate. Images of the sections were obtained with an HT-7800 transmission electron microscope (120 kV) equipped with a Complementary Metal-Oxide-Semiconductor camera (Hitachi, Tokyo, Japan).

### 2.4. GES-1 cells cultured with PS-NPs

GES-1 cells were obtained from the Laboratory of Pathogenic Biology of Binzhou Medical University. The cells were cultured in Dulbecco's modified Eagle's medium containing 10% fetal bovine serum in an incubator set with the following parameters: 5% $CO_2$ atmosphere and 37 °C (Song et al., 2019).

GES-1 cells were plated onto sterilized laser confocal dishes. Cells were incubated with PS-NPs (50 μg/mL, 500 μL) for 2, 4, 6, 12, 24, and 48 h. Nuclei were stained with DAPI. The cells were observed under a confocal laser scanning microscope (Suzuki et al., 1997).

Additionally, GES-1 cells were co-cultured with PS-NPs (50 μg/mL, 500 μL) for 24 h. The RhoA, Rac1, F-actin, Rab5, RAB7, LAMP1, LC3B II, and GAPDH protein levels in treated cells were analyzed by Western blot.

Cells were also co-cultured with PS-NPs (50 μg/mL, 500 μL) for 12, 24, and 48 h, and the cell proliferative rates, mitochondrial membrane potential ($\Delta\psi$), cell apoptosis rates, autophagy, and LC3II protein levels were detected by EdU, JC-1, Annexin V-FITC, adenovirus transfection, and Western blot assays, respectively.

### 2.5. Drug treatment in GES-1 cells cultured with PS-NPs

#### 2.5.1. Endocytosis inhibition test

The drugs nystatin (Nys), chlorpromazine HCl (Chl), and ethylisopropyl amiloride (EIPA) were used to inhibit caveolae-mediated endocytosis, clathrin-mediated endocytosis, and micropinocytosis, respectively. Briefly, cells were cultured with Nys (20 μM) for 2 h, Chl (3 μM) for 2 h, or EIPA (25 μM) for 30 min. GES-1 cells with no treatment constituted the Blank group. PS-NPs (50 μg/mL, 500 μL) were added to the cells. The fluorescence intensity of cells was observed and evaluated under a confocal laser scanning microscope (Dausend et al., 2008).

#### 2.5.2. RhoA and Rac1 inhibition assay

The inhibitors of Rac1 and RhoA were NSC 23766 (NSC) and CCG-1423 (CCG), respectively (Zhang et al., 2019). Cells were cultured with 50 μM of NSC or 5 μM of CCG for 1 h. GES-1 cells in Blank group had no treatment. PS-NPs (50 μg/mL, 500 μL) were added to the cells, and they were harvested and evaluated fluorescence intensity. The F-actin protein levels in GES-1 cells were analyzed by Western blot.

#### 2.5.3. F-actin depolymerization test

To analyze the involvement of the cytoskeleton when PS-NPs enter GES-1 cells, LantrunculinA (LatA) was used to inhibit F-actin polymerization (Chazotte, 2010). Cells were treated with 0.1 μM of LatA for 1 h. Cells in the Blank group had no treatment. PS-NPs (50 μg/mL, 500 μL) were added to the cells, and then the fluorescence intensity of cells was evaluated.

### 2.6. Western blot assay

Cells were lysed at 4 °C for 20 min in lysate buffer containing RIPA and PMSF. A BCA protein assay kit was used to detect the total protein concentration (Beyotime Biotechnology, Shanghai, China). Samples were separated on a 12% SDS-PAGE gel, and the bands on the gel subsequently were transferred onto polyvinylidene fluoride membranes (Millipore, Billerica, MA, USA). TBS-T buffer containing 6% skim milk was used to block the blots. Membranes were incubated overnight with primary antibodies (Abcam, Cambridge, MA, USA) following the manufacturer's instructions. After the blots were washed, they were then incubated with a horseradish peroxidase-conjugated secondary antibody (Cell Signaling Technology, Boston, MA, USA) for 60 min. Finally, antibody-bound proteins were detected using an electro-chemi-luminescence system (Beyotime Biotechnology) (Xu et al., 2019). GAPDH was used as the internal reference.

### 2.7. EdU cell proliferation assay

The proliferation of GES-1 cells was detected using an EdU proliferation detection kit (KeyGEN BioTECH, Nanjing, China) (Zhou et al., 2017). Briefly, 10 μM of EdU were added to the cells, which then were fixed with 4% paraformaldehyde, permeated with 0.5% Triton X-100, and stained with a Click-iT reaction mixture. The mixture was incubated with Hoechst33342 to stain nuclei (kFluor488: Ex/Em = 495/520 nm; Hoechst 33342: Ex/Em = 350/461 nm).

### 2.8. Cell apoptosis assays

Apoptosis of GES-1 cells was detected using an Annexin V-FITC/propidium iodide (PI) apoptosis detection kit (Invitrogen, Carlsbad, CA, USA) following the manufacturer's instructions (Zhu et al., 2017). The digested GES-1 cells were centrifuged at 1000 rpm for 5 min, and the precipitate was suspended with binding buffer, then incubated with 5 μL of Annexin V-FITC at room temperature for 10 min. The mixture was centrifuged again, and the precipitate was suspended with binding buffer with 5 μL of PI. And then apoptotic cells were detected by flow cytometry (BD, Franklin Lake, NJ, USA).

Cell apoptosis was analyzed using the JC-1 (5,5′,6,6′-tetrachloro-1,1′,3,3′-tetraethyl benzimidazole carbocyanine iodide) method. JC-1 was used to detect the $\Delta\psi$ of apoptotic cells, and the decrease of $\Delta\psi$ indicated the earliest event in the cascade reaction of apoptosis (Darzynkiewicz et al., 2001). After digestion, the cells were co-cultured with 500 μL of JC-1 working solution at 37 °C for 15 min, and then the assay buffer was added to the reaction. The mixture was centrifuged, and the precipitate was resuspended in assay buffer. The $\Delta\psi$ of apoptotic cells was detected by flow cytometry.

### 2.9. Adenovirus transfection

GES-1 cells were infected with mRFP-GFP-LC3 adenovirus (MOI = 1:200) and cultured with Opti-MEM for 12 h, then co-cultured with PS-NPs (50 μg/mL, 500 μL) for 12, 24, and 48 h. At each time point, cells were collected and fixed in 4% paraformaldehyde. The numbers of yellow spots (autophagosomes) and red spots (autolysosomes) were counted under an laser confocal microscope to analyze autophagy (Zhu et al., 2017).

### 2.10. Statistical analysis

The mean ± standard deviation (SD) was used to present the data from the five independent experiments. SPSS 22.0 software was used to perform one-way analysis of variance to determine statistical significance among groups. Pearson correlation coefficient was used to evaluate the relationship between intracellular fluorescence intensity and exposure time in GES-1 cells. $P < 0.05$ was considered to be statistically significant.

## 3. Results

### 3.1. Entry of PS-NPs into mice tissues and GES-1 cells

The distribution of PS-NPs in the gastric, intestine, liver, cardiac, spleen, and lung tissues of mice was detected. Compared with the Blank group, the fluorescence spots of PS-NPs were clearly visible in the gastric, intestine, and liver tissues of mice in the PS-NPs-treated group (Fig. 1A). No fluorescent particles were observed in the cardiac, spleen, and lung tissues (data not shown).

To further corroborate the distribution of PS-NPs in mouse tissues, the appearance of PS-NPs was investigated by transmission electron microscopy (Fig. 1B). PS-NPs were visible in gastric, intestine, and liver tissues of PS-NPs-treated mice, and no PS-NPs were observed in the cardiac, spleen, and lung tissues (data not shown).

The presence of fluorescent PS-NPs was observed in GES-1 cells co-treated with PS-NPs cells after 2, 4, 6, 12, 24, and 48 h (Fig. 1C). Pearson's correlation analysis was used to study the relationship between accumulation increase of NPs and exposure time in GES-1 cells. The correlation between intracellular fluorescence intensity and exposure time was statistically significantly positive ($R = 0.667$, $P < 0.01$); this result showed that the amount of PS-NPs accumulating in GES-1 cells increased with increasing exposure time.

### 3.2. Endocytic pathway of PS-NPs into GES-1 cells

To elucidate the endocytic pathway of PS-NPs, the drugs Nys, Chl, and EIPA were used as inhibitors of caveolae-mediated endocytosis, clathrin-mediated endocytosis, and micropinocytosis, respectively. The results showed that the numbers of PS-NPs entering GES-1 decreased with the addition of Nys, Chl, and EIPA. The average fluorescence intensity of GES-1 cells only treated with fluorescent PS-NPs was 29.26 ± 3.3, which was significantly higher ($P < 0.01$) than that in the PS-NPs groups pretreated with Nys, Chl, or EIPA. The fluorescence intensity of the Nys-pretreated PS-NPs group was 5.33 ± 0.44, which was significantly lower ($P < 0.05$) than that in the Chl-pretreated PS-NPs group (12.92 ± 1.99).

### 3.3. RhoA/F-actin signaling pathways regulating the internalization of PS-NPs in GES-1 cells

The drugs CCG, NSC, and LatA were used as inhibitors of RhoA, Rac1, and F-actin polymerization, respectively. The average fluorescence intensities of the PS-NPs, CCG-pretreatment PS-NPs, and NSC-pretreatment PS-NPs groups were 28.21 ± 3.61, 3.51 ± 1.42, and 30.61 ± 4.18, respectively (Fig. 3A and B). The average fluorescence intensity in the CCG-pretreatment PS-NPs group was remarkably lower ($P < 0.001$) than that in the PS-NPs group, and no significant difference in the average fluorescence intensity was found between the PS-NPs and NSC-pretreatment PS-NPs groups.

To determine whether F-actin polymerization was regulated by RhoA or Rac1, we investigated F-actin protein levels in GES-1 cells treated with Rac1 or RhoA inhibitors through Western blot. GES-1 cells pretreated with RhoA inhibitor had a significantly decreased F-actin protein level after PS-NPs treatment ($P < 0.05$). No significant difference was found between the other groups (Fig. 3C and D).

The average fluorescence intensities of the PS-NPs and LatA-

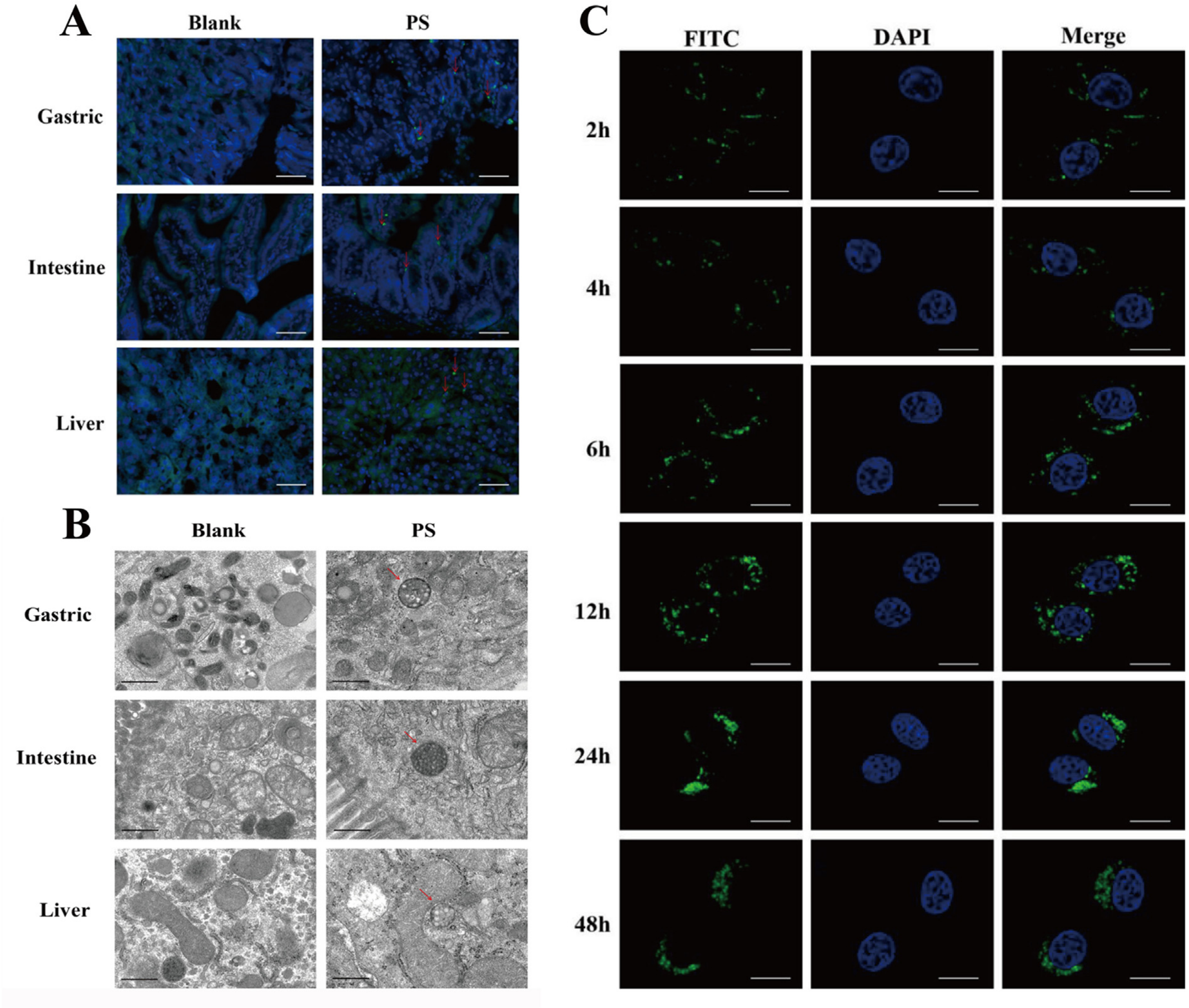

**Fig. 1.** PS-NPs entry into mice tissues and GES-1 cells. (A) Distribution of PS-NPs in the gastric, intestine, liver tissues of mice observed by fluorescence microscopy. The green color indicates PS-NPs, and the nuclei are blue (stained by DAPI). The red arrow indicates PS-NPs in mice. Scale bar: 20 μm. (B) Ultrastructural features of GES-1 cells were analyzed by transmission electron microscopy. Typical images of PS-NPs (red arrow) in gastric, intestine, and liver tissues are shown. Scale bar: 500 nm. (C) The presence of fluorescent PS-NPs in GES-1 cells co-treated with PS-NPs after 2, 4, 6, 12, 24, and 48 h. The green color indicates PS-NPs, and the nuclei are blue (stained by DAPI). (For interpretation of the references to color in this figure legend, the reader is referred to the Web version of this article.)

pretreatment PS-NPs groups were 23.67 ± 3.50 and 4.50 ± 1.97, respectively (Fig. 3E and F). The average fluorescence intensity in the LatA-pretreatment PS-NPs group was remarkably lower ($P < 0.001$) than that in the PS-NPs group.

### 3.4. *Transport pathway of PS-NPs after entering GES-1 cells*

To further determine the localization of PS-NPs in GES-1 cells, the distribution of PS-NPs in cells was observed by transmission electron microscopy (Fig. 4A). After the interaction between PS-NPs and GES-1 cells, PS-NPs were adsorbed onto cell vesicles and then entered the cells as protrusions and depressions of the cell membrane. Internalized PS-NPs can be encapsulated in vesicles, autophagosomes, lysosomes, and lysosomal residues.

The Rho GTPase family proteins (RhoA and Rac1), F-actin, transport-related protein (Rab5, RAB7, and LAMP1) levels were detected by Western blot analysis in PS-NPs-treated GES-1 cells (Fig. 4B–E). The RhoA level in PS-NPs-treated GES-1 cells was significantly higher ($P < 0.01$) than that in untreated cells. No significant difference in Rac1 levels was observed between PS-NPs-treated and untreated groups. The F-actin level in PS-NPs-treated GES-1 cells was remarkably up-regulated compared to that in the Blank group ($P < 0.05$). The Rab5 level was significantly lower ($P < 0.05$) and RAB7 and LAMP1 levels were significantly higher in the PS-NPs-treated group compared to those in the control group without treatment ($P < 0.05$).

### 3.5. *PS-NPs down-regulated cell proliferation rates of GES-1 cells*

No significant change in cell proliferation was observed after treatment with PS-NPs at 12 h. Cell proliferation rates were 18.52 ± 1.96% and 21.76 ± 1.91% after 24 and 48 h of treatment with PS-NPs, respectively, which were significantly lower ($P < 0.01$) than those in the Blank group (Fig. 5).

### 3.6. *PS-NPs up-regulated apoptosis in GES-1 cells*

The apoptosis of GES-1 cells was significantly up-regulated after cells were treated with PS-NPs for 12 and 24 h (Fig. 6A and B). At 12 and 24 h, cell apoptosis increased to 11.40 ± 1.59% and 18.90 ± 2.08%, respectively. No significant difference in apoptosis between the Blank and PS-NPs-treatment group was detected after

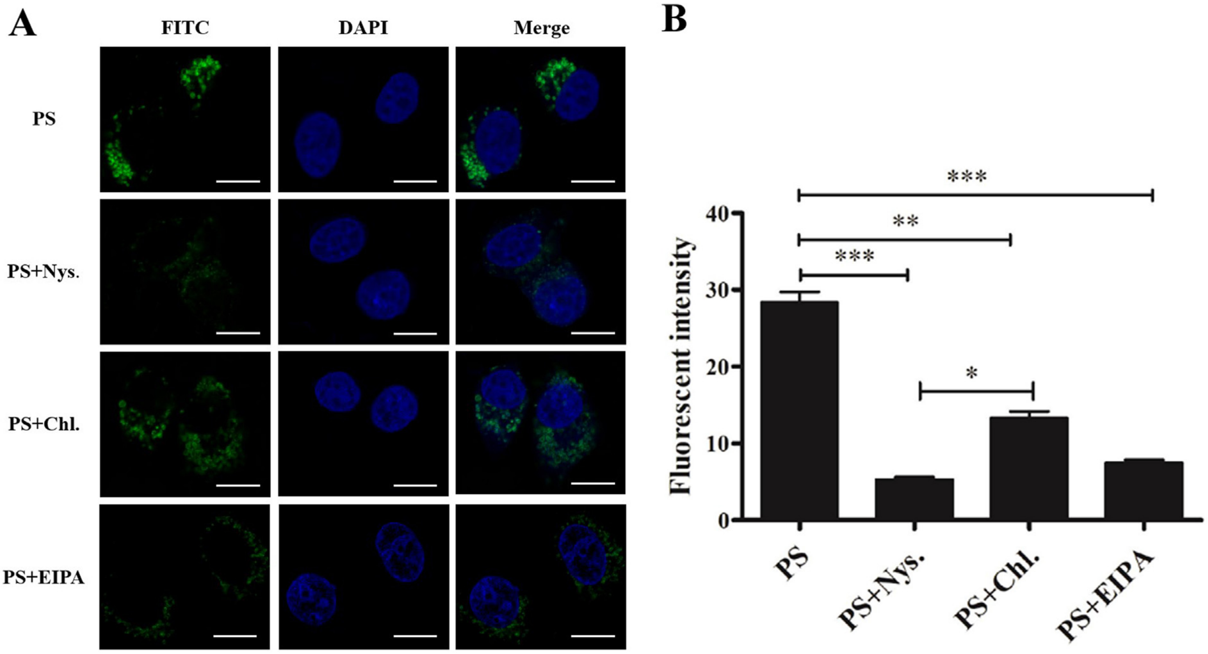

**Fig. 2.** The drugs Nys, Chl, and EIPA inhibited the entry of PS-NPs into GES-1 cells. (A) Fluorescent PS-NPs in cells treated with Nys, Chl, and EIPA. The green color indicates PS-NPs, and the nuclei are blue (stained by DAPI). (B) Fluorescence intensity in PS-NPs, Nys-pretreated PS-NPs, Chl-pretreated PS-NPs, and EIPA-pretreated PS-NPs. Mean ± SD of 30 cells. $*P < 0.05$; $**P < 0.01$; $***P < 0.001$. (For interpretation of the references to color in this figure legend, the reader is referred to the Web version of this article.)

48 h.

JC-1 was used to detect the $\Delta\psi$ of apoptotic cells; a decrease in $\Delta\psi$ is the earliest event in the apoptotic cascade. GES-1 cells treated with PS-NPs displayed $\Delta\psi$ of 1.97 ± 0.84 and 1.24 ± 0.53 at 12 and 24 h after treatment, respectively. There was a remarkable decrease ($P < 0.05$) in the PS-NPs-treatment group compared with the Blank group. There was no statistical significance in $\Delta\psi$ between the Blank and PS-NPs-treatment group at 48 h.

### 3.7. PS-NPs induced autophagy in GES-1 cells

The formation of autophagosomes and autolysosomes was analyzed using the tandem mRFP-GFP-LC3B adenovirus. We found that the numbers of yellow fluorescent autophagosomes and red fluorescent autolysosomes were both higher in the PS-NPs-treatment group compared with the Blank group at 12, 24, and 48 h after treatment (Fig. 7A—C). The formation of autophagosomes and autolysosomes was time-dependent and increased with the length of PS-NPs treatment. The numbers of autophagosomes and autolysosomes were highest 48 h after treatment with PS-NPs. Their values were 22.71 ± 6.18 and 73.29 ± 18.09 per cell, respectively, which were 2.37-fold and 40.72-fold higher ($P < 0.01$) in the PS-NPs-treatment group compared to the Blank group, respectively.

To further investigate the effect of PS-NPs on autophagy, the autophagy marker protein LC3II level was detected by Western blot assay. LC3 II levels were significantly up-regulated ($P < 0.01$) at 12, 24, and 48 h after PS-NPs treatment (Fig. 7D and E). These results indicate that PS-NPs induced autophagy in GES-1 cells.

## 4. Discussion

Due to their large surface area-volume ratios and smaller particle sizes, nanoparticles can easily pass through GI barriers and enter the circulation system, which will eventually lead to systemic exposure. Wang et al. (2013) found that a small amount of ZnO nanoparticles could enter the circulatory system and accumulate in some organs, such as the liver. Smith et al. (2013) demonstrated GI absorption of 2.0 nm diameter gold nanoparticles. In this study, PS-NPs were clearly visible in the gastric, intestine, and liver tissues of mice treated with PS-NPs (Fig. 1A and B), but no PS-NPs were observed in the cardiac, spleen, and lung tissues (data not shown). Deng et al. (2017) exposed mice to microplastics with particle sizes of 5 and 20 μm, which resulted in decreased liver ATP levels and lipid metabolism and increased lactate dehydrogenase levels. Therefore, the accumulation of PS-NPs in gastric, intestine, and liver tissues of mice might not only destroy the integrity of GI tissues and produce an oxidative stress response, but it also might disrupt liver function, including energy metabolism. PS-NPs in other tissues were not observed in this study, which might be related to low exposure time, dose, or undetectable levels in the tissues. Subsequent research should further explore the accumulation of PS-NPs in other tissues by prolonging the exposure time. The results above indicated that PS-NPs could enter GI tissues and lead to exposure of distal tissues, such as the liver.

We observed fluorescent PS-NPs in GES-1 cells co-cultured with PS-NPs after 2, 4, 6, 12, 24, and 48 h (Fig. 1C). We also obtained statistically significant positive correlations (R = 0.667, $P < 0.01$) between intracellular fluorescence intensity of PS-NPs and exposure time; thus the amounts of PS-NPs that accumulated in GES-1 cells increased with increasing exposure time. Xu et al. (2019) found that NPs (diameter: 25 nm and 70 nm) could be internalized in human A549 cells, and the internalization rates increased with the length of treatment time. Schirinzi et al. (2017) found that 0.05—10 mg of polystyrene (40—250 nm) and polyethylene (100—600 nm) NPs induced human epithelial cell dissolution, increased reactive oxygen species (ROS) production, and caused cytotoxicity. Moreover, exposure of human macrophages and lung epithelial cells to PS-NPs (60 nm) led to ROS production, endoplasmic reticulum stress (caused by misfolded protein aggregation), and even autophagy (Chiu et al., 2015).

Endocytosis is considered to be the main mechanism in the

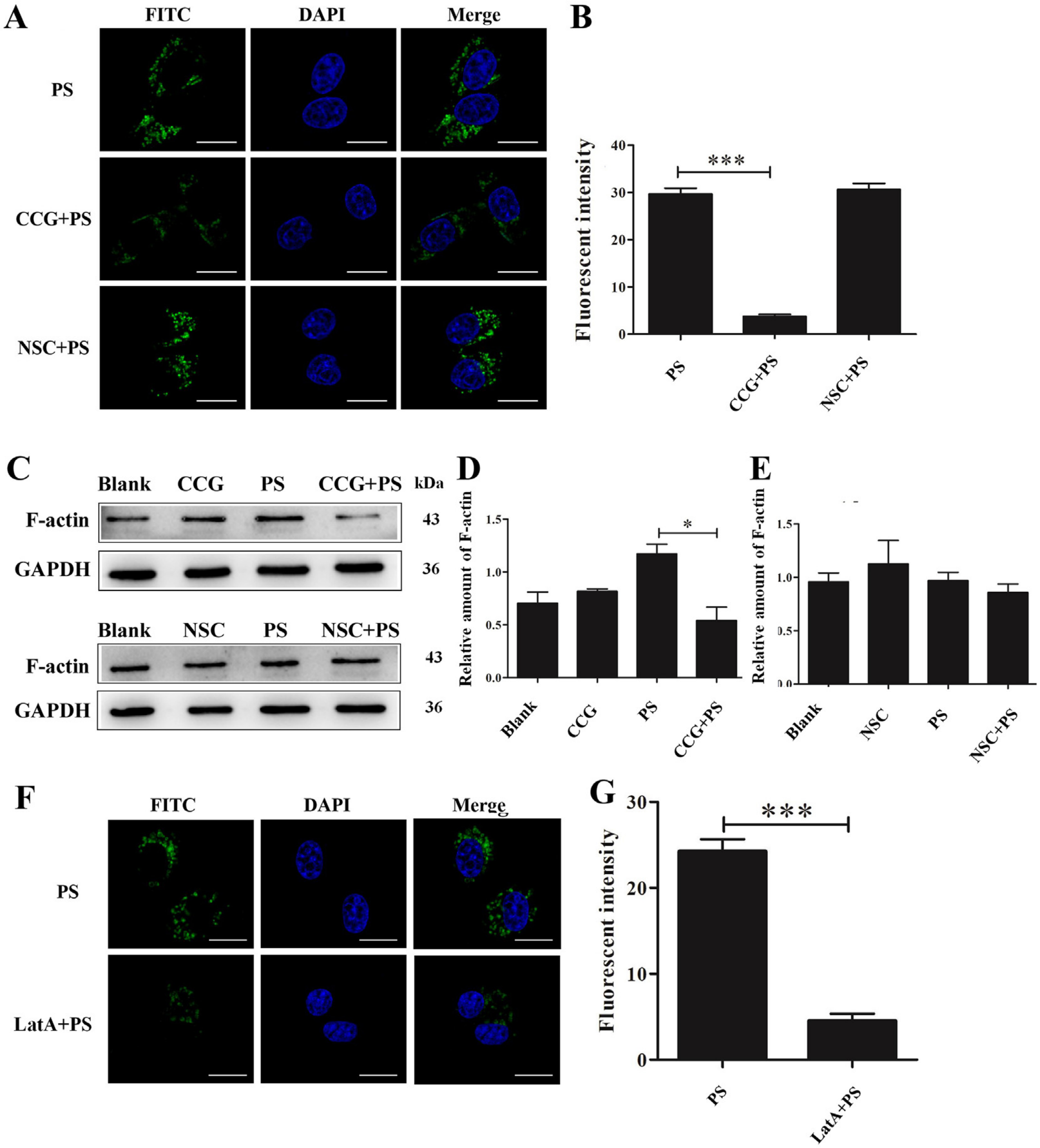

**Fig. 3.** The effect of CCG and NSC on PS-NPs entry into GES-1 cells. (A) Fluorescent PS-NPs in cells treated with CCG and NSC. The green color indicates PS-NPs, and the nuclei are blue (stained by DAPI). (B) Fluorescence intensity in PS, CCG-pretreated PS-NPs, and NSC-pretreated PS-NPs. Mean ± SD of 30 cells. *$P < 0.05$; **$P < 0.01$; ***$P < 0.001$. (C) F-actin protein levels in the control, PS-NPs, CCG-pretreated PS-NPs, and NSC-pretreated PS-NPs groups determined by Western blot anaylsis. (D) Densitometric analyses show the differences among the control, PS-NPs, CCG, and CCG-pretreated PS-NPs groups. (E) Densitometric analyses show the differences among the control PS-NPs, NSC, and NSC-pretreated PS-NPs groups. (F) The presence of fluorescent PS-NPs in cells treated with LatA. The green color indicates PS-NPs, and the nuclei are blue (stained by DAPI). (G) Fluorescence intensity in PS and LatA-pretreated PS-NPs groups. Mean ± SD of 30 cells. *$P < 0.05$; ***$P < 0.001$. (For interpretation of the references to color in this figure legend, the reader is referred to the Web version of this article.)

transcellular pathway of nanoparticles passing through epithelial cells (Shang et al., 2014; Zhao et al., 2011). The endocytosis of nanoparticles involves a variety of protein-mediated pathways, including clathrin and caveolae-mediated endocytosis and macropinocytosis. The present study showed that the numbers of PS-NPs entering cells decreased with the addition of Nys, Chl, and EIPA (Fig. 2). In other words, after the inhibition of clathrin-mediated endocytosis and caveolin-mediated endocytosis, as well as megacytosis, the cell internalization rates of PS-NPs decreased. However, inhibition of one endocytosis or macropinocytosis pathway alone could not completely block the cellular internalization of PS-NPs, which indicated that PS-NPs entered host cells through multiple endocytosis or macropinocytosis pathways. Kuhn et al. (2014) have shown that PS nanoparticles with a diameter of 40 nm can be taken up by macrophages through macropinocytosis, phagocytosis, and clathrin-mediated endocytosis. In this study, the cell internalization rate of PS-NPs after inhibiting caveolae-mediated endocytosis was lower ($P < 0.05$) than that after clathrin-mediated endocytosis. The differences above might be due to different characteristics in the abundance of endocytosis related proteins in different cell types. For example, adipocytes, smooth muscle cells, epithelial cells, and endothelial cells are known to be rich in caveolae (Parton and Simons, 2007). In summary, our results demonstrated that PS-NPs entering GES-1 cells could rely on clathrin and caveolae-mediated endocytosis and macropinocytosis, of which caveolin-mediated endocytosis was more likely to promote the cell internalization of PS-NPs.

The Rho GTPase family regulates the actin cytoskeleton to affect

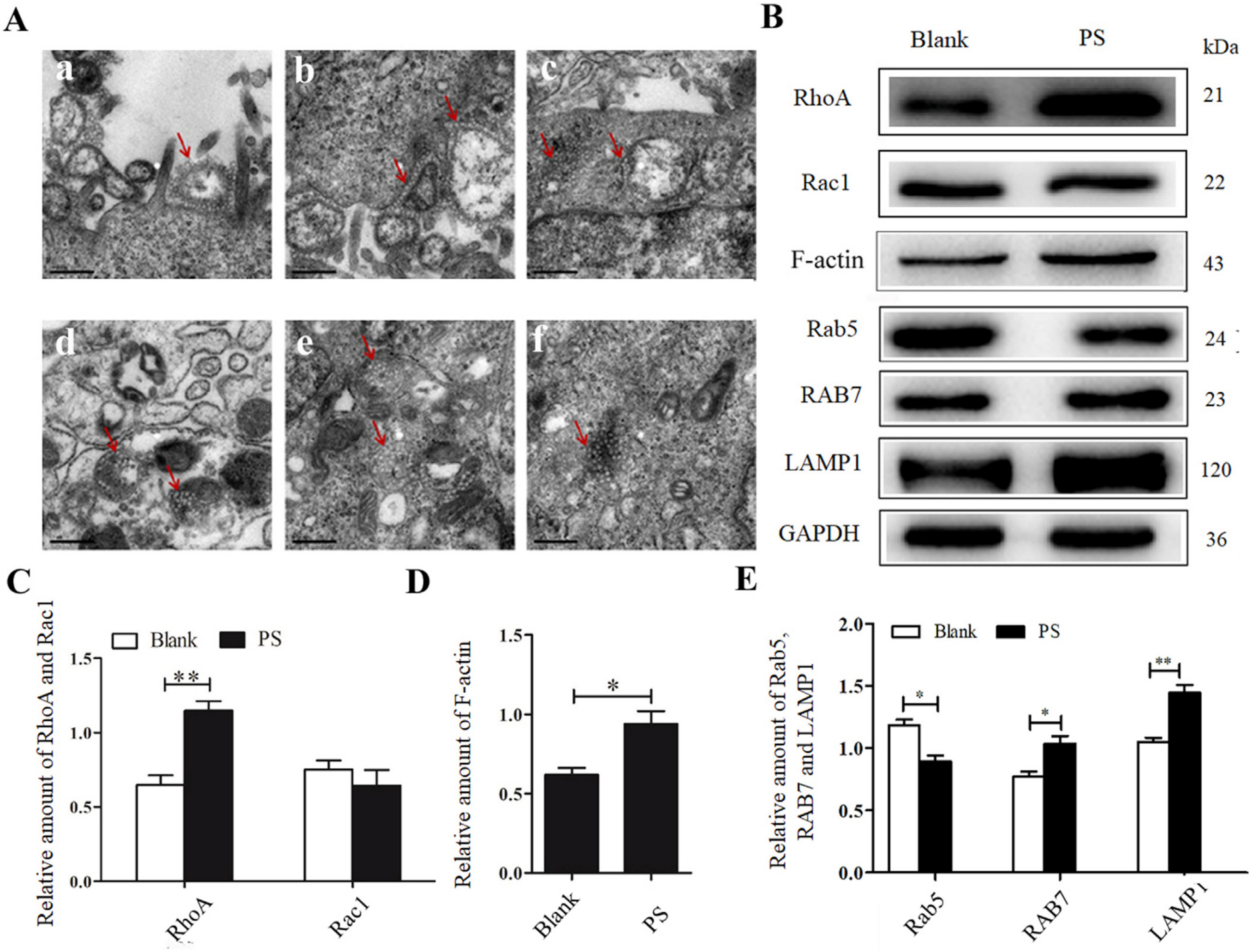

**Fig. 4.** Pathway of PS-NPs after entering GES-1 cells. (A) Ultrastructural features of cells treated with PS-NPs were analyzed by transmission electron microscopy. PS-NPs were adsorbed onto (a) cell vesicles and entered cells as protrusions, and then (b) depression of the cell membrane. Internalized PS-NPs can be encapsulated in (c) vesicles, (d) autophagosomes, (e) lysosomes, and (f) lysosomal residues. The red arrow indicates PS-NPs. Scale bar: 500 nm. (B) The RhoA, Rac1, F-actin, Rab5, RAB7, and LAMP1 protein levels were detected by Western blot assay. Densitometric analyses show the differences in the (C) RhoA and Rac1, (D) F-actin, and (E) Rab5, RAB7, and LAMP1 protein levels between the control and PS-NPs group. Mean ± SD of five independent assays. $*P < 0.05$; $**P < 0.01$. (For interpretation of the references to color in this figure legend, the reader is referred to the Web version of this article.)

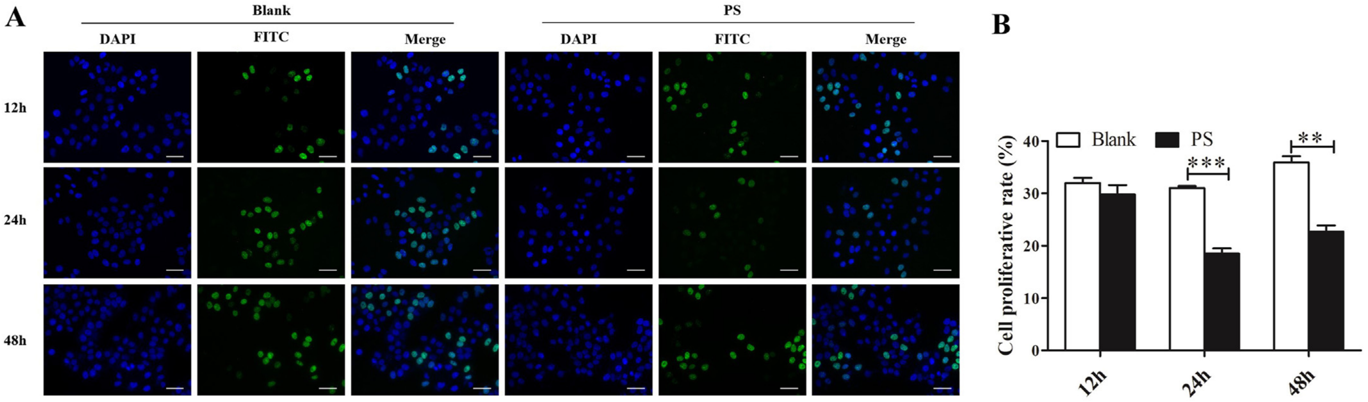

**Fig. 5.** Proliferation of GES-1 cells treated with PS-NPs determined using the EdU staining assay. Fluorescence microscopy was used to detect EdU incorporation. Typical photomicrographs (A) and cell proliferation rates (B) are shown. Mean ± SD of five independent assays. $**P < 0.01$; $***P < 0.001$.

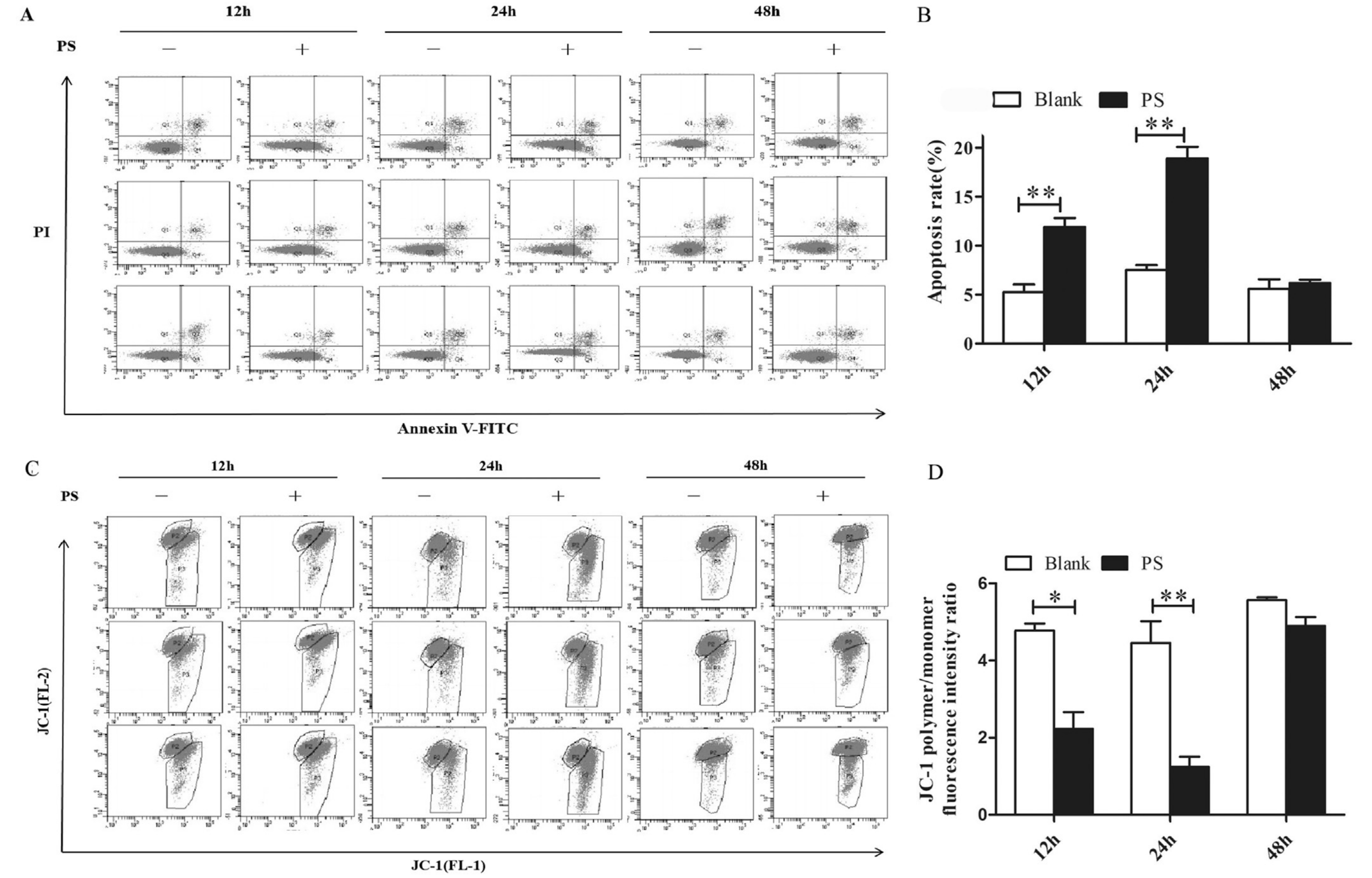

**Fig. 6.** Flow cytometry analysis of apoptosis of GES-1 cells treated with PS-NPs. Annexin V-FITC/PI double staining was employed to evaluate cell apoptosis. Typical flowcharts (A) and cell apoptotic rates (B) are shown. Mitochondrial membrane potential ($\Delta\psi$) in cells treated with PS-NPs was detected by JC-1. Representative flowcharts (C) and JC-1 polymer/monomer ($\Delta\psi$) fluorescence intensity ratio (D) are shown. Mean ± SD of five independent assays. $^{**}P < 0.01$.

multiple cellular processes, such as endocytosis, which is actin-dependent. The activation of the Rho GTPase family members induces endocytosis by altering the formation of actin stress fibers or filaments (Croisé et al., 2014; Miao et al., 2018). The drugs CCG, NSC, and LatA were used as inhibitors of RhoA, Rac1, and F-actin polymerization, respectively, in the present study. The average fluorescence intensities of PS-NPs pretreated with either CCG or LatA were remarkably lower ($P < 0.001$) than that in untreated PS-NPs, and no significant difference in the average fluorescence intensity was found between untreated PS-NPs and PS-NPs pretreated with NSC (Fig. 3). The protein level of F-actin was significantly decreased in the PS-NPs group pretreated with RhoA inhibitor compared to the GES-1 cells treated with PS-NPs alone ($P < 0.05$). These results suggested that RhoA/F-actin signaling pathways promoted the endocytosis of PS-NPs in GES-1 cells.

To further investigate the localization of PS-NPs in GES-1 cells, the distribution of PS-NPs in cells was observed by transmission electron microscopy (Fig. 4A). PS-NPs were adsorbed onto cell vesicles and then entered the cell as a protrusion and depression of the cell membrane. Internalized PS-NPs can be encapsulated in vesicles, autophagosomes, lysosomes, and lysosomal residues. Wang et al. (2018) also observed the accumulation of nanoparticles in lysosomes after exposure to PS nanoparticles in mouse embryonic fibroblast cells for 3 h. Yang et al. (2019) found that 150 nm of $ZrO_2$ persisted in lysosomes of macrophages but decreased after 4 weeks, suggesting that $ZrO_2$ can be excreted from the cell. However, the PS-NPs in this study were found in lysosomal residues, indicating that enzymes in the lysosomes of GES-1 cells could not degrade and digest PS-NPs. Intracellular transport generally starts from the early endosome to the late endosome and fuses with lysosomes eventually, a process closely related to Rab family proteins (Ao et al., 2014). Rab5, RAB7, and LAMP1 are the major regulatory proteins of early endosomes, late endosomes, and lysosomes, respectively (Hofmann et al., 2014; Stenmark, 2009). In the present study, the RhoA, F-actin, RAB7, and LAMP1 levels in PS-NPs-treated GES-1 cells were remarkably up-regulated and the Rab5 level was significantly down-regulated compared to that in the Blank group ($P < 0.05$) (Fig. 4B–E). Similarly, nanoparticle SiNPs were taken up by L-02 and HepG2 cells and were observed to be distributed in the cytoplasm, lysosomes, and autophagic vacuoles (Wang et al., 2017). The present study indicated that PS-NPs regulated endocytosis through the RhoA/F-actin signaling pathway in cells, and internalized PS-NPs went through early and late endosomes, and finally existed in the cytoplasm, autophagosomes, or lysosomes.

The accumulation of NPs in organisms can cause biological toxicity, such as organelle aggregation, cellular oxidative damage, mitochondrial depolarization, and cytotoxicity (Guilhermino et al., 2018; Sendra et al., 2019). In this study, the effects of PS-NPs on cell proliferation, cell apoptosis, and autophagy were investigated. The results showed that PS-NPs decreased cell proliferation rates and increased cell apoptosis (Figs. 5 and 6). PS-NPs inhibited cell proliferation and promoted cell apoptosis in a time-dependent manner. Xu et al. (2019) indicated that NPs could significantly induce cell apoptosis after they were internalized in A549 cells. In

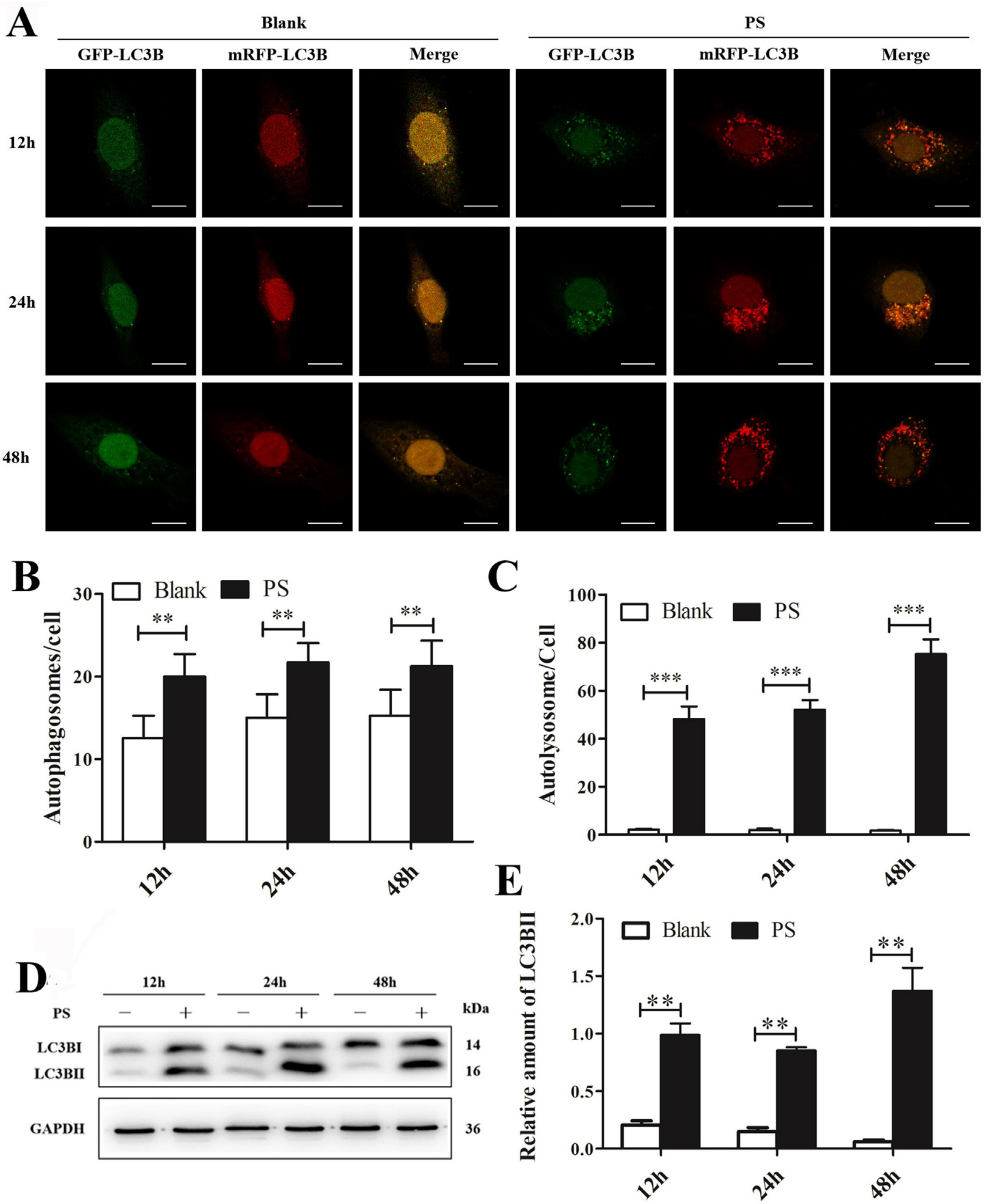

**Fig. 7.** PS-NPs induced cell autophagy in GES-1 cells. (A) GES-1 cells were treated with PS-NPs for 12, 24, and 48 h after transfection with mRFP-GFP-LC3B adenovirus. Scale bar: 20 μm. (B) Autophagosome and (C) autolysosome numbers were counted. Mean ± SD of 30 cells. (D) LC3II levels in GES-1 cells after PS-NPs treatment by Western blot analysis. (E) Densitometric analyses show the differences in LC3II levels between the Blank and PS group. Mean ± SD of five independent assays. **$P < 0.01$.

addition, the formation of autophagosomes and autolysosomes is time-dependent and increased with prolonged PS-NPs treatment (Fig. 7). The results indicated that PS-NPs induced autophagy in GES-1 cells. Wang et al. (2017) also showed that SiNPs could promote the accumulation of autophagosomes in dose- and time-dependent manners in L-02 and HepG2 cells. Furthermore, in both cancerous and glioma cells, nanoparticles have been shown to induce cytoprotective autophagy (Lin et al., 2014; Wu et al., 2015). In short, PS-NPs had cytotoxic effects on GES-1 cells.

## 5. Conclusions

In summary, we found that PS-NPs were clearly visible in the gastric, intestine, and liver tissues of mice after 3 d of PS-NPs treatment, and their entry into GES-1 cells was time-dependent. PS-NPs may enter GES-1 cells via clathrin, micropinocytosis, and caveolae-mediated endocytosis, and the latter may be most likely to promote cell internalization. PS-NPs regulate endocytosis through the RhoA/F-actin signaling pathway in cells, and internalized PS-NPs went through early and late endosomes, and were finally retained in the cytoplasm, autophagosomes, or lysosomes. On entering cells, PS-NPs inhibited cell proliferation, promoted apoptosis, and induced autophagy to produce cytotoxicity.

## Funding

This work was supported by the National Natural Science Foundation of China (grant number 42077402) and the Department of Education of Shandong Province (grant number 2019KJK012).

## Author statement

**Yunfei Ding**: Methodology and Investigation. **Ruiqing Zhang**: Investigation and Writing – original draft. **Boqing Li**: Visualization and Resources. **Yunqiu Du**: Visualization and Software. **Jing Li**: Formal analysis. **Xiaohan Tong**: Software. **Yulong Wu**: Data curation. **Xiaofei Ji**: Data curation. **Ying Zhang**: Conceptualization, Writing – review & editing, Project administration and Funding acquisition.

## Declaration of competing interest

The authors declare that they have no known competing financial interests or personal relationships that could have appeared to influence the work reported in this paper.

## Acknowledgement

We thank International Science Editing (http://www.internationalscienceediting.com) for editing this manuscript.

## References

Ao, X., Zou, L., Wu, Y., 2014. Regulation of autophagy by the Rab GTPase network. Cell Death Differ. 21, 348–358.

Busch, M., Bredeck, G., Kämpfer, A., Schins, R., 2021. Investigations of acute effects of polystyrene and polyvinyl chloride micro- and nanoplastics in an advanced in vitro triple culture model of the healthy and inflamed intestine. Environ. Res. 193, 110536.

Chazotte, B., 2010. Labeling cytoskeletal F-actin with rhodamine phalloidin or fluorescein phalloidin for imaging. Cold Spring Harb. Protoc. 2010 (5).

Chiu, H.W., Xia, T., Lee, Y.H., Chen, C.W., Tsai, J.C., Wang, Y.J., 2015. Cationic polystyrene nanopheres induce autophagic cell death through the induction of endoplasmic reticulum stress. Nanoscale 7, 736–746.

Contado, C., 2015. Nanomaterials in consumer products: a challenging analytical problem. Front. Chem. 3, 48.

Croisé, P., Estay-Ahumada, C., Gasman, S., Ory, S., 2014. Rho GTPases, phosphoinositides, and actin: a tripartite framework for efficient vesicular trafficking. Small GTPases 5, e29469.

Darzynkiewicz, Z., Bedner, E., Smolewski, P., 2001. Flow cytometry in analysis of cell cycle and apoptosis. Semin. Hematol. 38, 179–193.

Dausend, J., Musyanovych, A., Dass, M., Walther, P., Schrezenmeier, H., Landfester, K., Mailänder, V., 2008. Uptake mechanism of oppositely charged fluorescent nanoparticles in HeLa cells. Macromol. Biosci. 8 (12), 1135–1143.

Deng, Y., Zhang, Y., Lemos, B., Ren, H., 2017. Tissue accumulation of microplastics in mice and biomarker responses suggest widespread health risks of exposure. Sci. Rep. 7, 46687.

Domenech, J., Hernández, A., Rubio, L., Marcos, R., Cortés, C., 2020. Interactions of polystyrene nanoplastics with in vitro models of the human intestinal barrier. Arch. Toxicol. 94 (9), 2997–3012.

Eleftheriadou, M., Pyrgiotakis, G., Demokritou, P., 2017. Nanotechnology to the rescue: using nano-enabled approaches in microbiological food safety and quality. Curr. Opin. Biotechnol. 44, 87–93.

Gewert, B., Plassmann, M.M., MacLeod, M., 2015. Pathways for degradation of plastic polymers floating in the marine environment. Environ. Sci. Process. Impacts. 17, 1513–1521.

Gigault, J., Halle, A.T., Baudrimont, M., Pascal, P.Y., Gauffre, F., Phi, T.L., El Hadri, H., Grassl, B., Reynaud, S., 2018. Current opinion: what is a nanoplastic? Environ. Pollut. 235, 1030–1034.

Guilhermino, L., Vieira, L.R., Ribeiro, D., Tavares, A.S., Cardoso, V., Alves, A., Almeida, J.M., 2018. Uptake and effects of the antimicrobial florfenicol, microplastics and their mixtures on freshwater exotic invasive bivalve Corbicula fluminea. Sci. Total Environ. 622–623, 1131–1142.

He, Y., Li, J., Chen, J., Miao, X., Li, G., He, Q., Xu, H., Li, H., Wei, Y., 2020. Cytotoxic effects of polystyrene nanoplastics with different surface functionalization on human HepG2 cells. Sci. Total Environ. 723, 138180.

Hofmann, D., Tenzer, S., Bannwarth, M.B., Messerschmidt, C., Glaser, S.F., Schild, H., Landfester, K., Mailänder, V., 2014. Mass spectrometry and imaging analysis of nanoparticle-containing vesicles provide a mechanistic insight into cellular trafficking. ACS Nano 8, 10077–10088.

Hillery, A.M., Jani, P.U., Florence, A.T., 1994. Comparative, quantitative study of lymphoid and non-lymphoid uptake of 60 nm polystyrene particles. J. Drug Target. 2 (2), 151–156.

Kashiwada, S., 2006. Distribution of nanoparticles in the see-through medaka (Oryzias latipes). Environ. Health Perspect. 114, 1697–1702.

Kuhn, D.A., Vanhecke, D., Michen, B., Blank, F., Gehr, P., Petri-Fink, A., Rothen-Rutishauser, B., 2014. Different endocytotic uptake mechanisms for nanoparticles in epithelial cells and macrophages. Beilstein J. Nanotechnol. 5, 1625–1636.

Lehner, R., Weder, C., Petri-Fink, A., Rothen-Rutishauser, B., 2019. Emergence of nanoplastic in the environment and possible impact on human health. Environ. Sci. Technol. 53 (4), 1748–1765.

Lin, J., Huang, Z., Wu, H., Zhou, W., Jin, P., Wei, P., Zhang, Y., Zheng, F., Zhang, J., Xu, J., Hu, Y., Wang, Y., Li, Y., Gu, N., Wen, L., 2014. Inhibition of autophagy enhances the anticancer activity of silver nanoparticles. Autophagy 10, 2006–2020.

Lu, Y., Zhang, Y., Deng, Y., Jiang, W., Zhao, Y., Geng, J., Ding, L., Ren, H.Q., 2016. Uptake and accumulation of polystyrene microplastics in zebrafish (*Danio rerio*) and toxic effects in liver. Environ. Sci. Technol. 50, 12523–12524.

Miao, Y., Tipakornsaowapak, T., Zheng, L., Mu, Y., Lewellyn, E., 2018. Phospho-regulation of intrinsically disordered proteins for actin assembly and endocytosis. FEBS J. 285, 2762–2784.

Parton, R.G., Simons, K., 2007. The multiple faces of caveolae. Nat. Rev. Mol. Cell Biol. 8, 185–194.

Prata, J.C., 2018. Airborne microplastics: consequences to human health? Environ. Pollut. 234, 115–126.

Schirinzi, G.F., Pérez-Pomeda, I., Sanchís, J., Rossini, C., Farré, M., Barceló, D., 2017. Cytotoxic effects of commonly used nanomaterials and microplastics on cerebral and epithelial human cells. Environ. Res. 159, 579–587.

Sendra, M., Staffieri, E., Yeste, M.P., Moreno-Garrido, I., Gatica, J.M., Corsi, I., Blasco, J., 2019. Are the primary characteristics of polystyrene nanoplastics responsible for toxicity and ad/absorption in the marine diatom *Phaeodactylum tricornutum*? Environ. Pollut. 249, 610–619.

Shang, L., Nienhaus, K., Nienhaus, G.U., 2014. Engineered nanoparticles interacting with cells: size matters. J. Nanobiotechnol. 12, 5.

Smith, C.A., Simpson, C.A., Kim, G., Carter, C.J., Feldheim, D.L., 2013. Gastrointestinal bioavailability of 2.0 nm diameter gold nanoparticles. ACS Nano 27, 3991–3996.

Son, A.I., Sokolowski, K., Zhou, R., 2013. Cryosectioning. Methods Mol. Biol. 1018, 301–311.

Song, H., Zhou, L., Liu, D., Ge, L., Li, Y., 2019. Probiotic effect on Helicobacter pylori attachment and inhibition of inflammation in human gastric epithelial cells. Exp. Ther. Med. 18 (3), 1551–1562.

Song, Y.K., Hong, S.H., Jang, M., Han, G.M., Jung, S.W., Shim, W.J., 2017. Combined effects of UV exposure duration and mechanical abrasion on microplastic fragmentation by polymer type. Environ. Sci. Technol. 51, 4368–4376.

Stenmark, H., 2009. Rab GTPases as coordinators of vesicle traffic. Nat. Rev. Mol. Cell Biol. 10, 513–525.

Suzuki, T., Fujikura, K., Higashiyama, T., Takata, K., 1997. DNA staining for fluorescence and laser confocal microscopy. J. Histochem. Cytochem. 45, 49–53.

Tizro, P., Choi, C., Khanlou, N., 2019. Sample preparation for transmission electron microscopy. Methods Mol. Biol. 1897, 417–424.

Walczak, A.P., Kramer, E., Hendriksen, P.J., Helsdingen, R., van der Zande, M., Rietjens, I.M., Bouwmeester, H., 2015. In vitro gastrointestinal digestion increases the translocation of polystyrene nanoparticles in an in vitro intestinal co-culture model. Nanotoxicology 9 (7), 886–894.

Wang, H., Du, L.J., Song, Z.M., Chen, X.X., 2013. Progress in the characterization and safety evaluation of engineered inorganic nanomaterials in food. Nanomedicine 8, 2007–2025.

Wang, J., Yu, Y., Lu, K., Yang, M., Li, Y., Zhou, X., Sun, Z., 2017. Silica nanoparticles induce autophagy dysfunction via lysosomal impairment and inhibition of autophagosome degradation in hepatocytes. Int. J. Nanomed. 12, 809–825.

Wang, F., Salvati, A., Boya, P., 2018. Lysosome-dependent cell death and deregulated autophagy induced by amine-modified polystyrene nanoparticles. Open. Biol. 8, 170271.

Wilkinson, J., Hooda, P.S., Barker, J., Barton, S., Swinden, J., 2017. Occurrence, fate and transformation of emerging contaminants in water: an overarching review of the field. Environ. Pollut. 231, 954–970.

Wu, H., Lin, J., Liu, P., Huang, Z., Zhao, P., Jin, H., Wang, C., Wen, L., Gu, N., 2015. Is the autophagy a friend or foe in the silver nanoparticles associated radiotherapy for glioma? Biomaterials 62, 47–57.

Xu, M., Halimu, G., Zhang, Q., Song, Y., Fu, X., Li, Y., Li, Y., Zhang, H., 2019. Internalization and toxicity: a preliminary study of effects of nanoplastic particles on human lung epithelial cell. Sci. Total Environ. 694, 133794.

Yang, Y., Bao, H., Chai, Q., Wang, Z., Sun, Z., Fu, C., Liu, Z., Liu, Z., Meng, X., Liu, T., 2019. Toxicity, biodistribution and oxidative damage caused by zirconia nanoparticles after intravenous injection. Int. J. Nanomed. 14, 5175–5186.

Yousif, E., Haddad, R., 2013. Photodegradation and photostabilization of polymers, especially polystyrene: review. SpringerPlus 2, 398.

Zhao, Y., Sun, X., Zhang, G., Trewyn, B.G., Slowing, I.I., Lin, V.S., 2011. Interaction of mesoporous silica nanoparticles with human red blood cell membranes: size and surface effects. ACS Nano 5, 1366–1375.

Zhang, C., Qiao, H., Guo, W., Liu, Y., Yang, L., Liu, Y., Jin, B., Fu, M., Wang, G., Li, W., 2019. CD100-plexin-B1 induces epithelial-mesenchymal transition of head and neck squamous cell carcinoma and promotes metastasis. Canc. Lett. 455, 1–13.

Zhou, Z., Yin, Y., Chang, Q., Sun, G., Lin, J., Dai, Y., 2017. Downregulation of B-myb promotes senescence via the ROS-mediated p53/p21 pathway, in vascular endothelial cells. Cell Prolif 50, e12319.

Zhu, P., Xue, J., Zhang, Z.J., Jia, Y.P., Tong, Y.N., Han, D., Li, Q., Xiang, Y., Mao, X.H., Tang, B., 2017. *Helicobacter pylori* VacA induces autophagic cell death in gastric epithelial cells via the endoplasmic reticulum stress pathway. Cell Death Dis. 8, 3207.